ROYAL SOCIETY
OF CHEMISTRY

PAPER

Check for updates

A high performance UV–visible dual-band photodetector based on an inorganic Cs_2SnI_6 perovskite/ZnO heterojunction structure

Dali Shao, [iD] *[a] Weiguang Zhu,[b] Guoqing Xin,[b] Xueqing Liu,[a] Tianmeng Wang,[ac] Sufei Shi, [iD] [ac] Jie Lian [iD] *[b] and Shayla Sawyer*[a]

Inorganic metal halide (IMH) perovskites have recently emerged as highly promising optoelectronic materials due to their excellent material properties, including tunable direct bandgap, long carrier diffusion length, high carrier mobility and outstanding environmental stabilities. However, the performance of photodetectors fabricated from IMH perovskites so far is limited as compared to their counterparts based on organic–inorganic hybrid perovskites. In this work, we demonstrate a high performance ultraviolet–visible (UV–Vis) dual-band photodetector based on a Cs_2SnI_6/ZnO heterojunction structure. By adjusting the polarity of the applied bias voltage, the photodetector can switch between two operation modes: (1) UV–Vis dual-band detection mode and (2) visible-blind UV detection mode. High detectivity in both the UV (1.39×10^{12} Jones) and visible (5.88×10^{11} Jones) regions is achieved. In addition, this photodetector demonstrated a fast response speed with a rise and fall time on the order of milliseconds and a large linear dynamic range of 119 dB. The excellent performance of this photodetector originates from efficient charge separation at the heterojunction interfaces, which will be discussed in detail in terms of the energy band diagrams and carrier dynamics of the device. Our study demonstrates the great application potential of inorganic vacancy-ordered perovskites in high-performance heterojunction photodetectors.

Introduction

Organic–inorganic hybrid perovskites have been considered to be promising for future optoelectronic applications due to their many excellent material properties including tunable direct bandgap, large optical absorption coefficients, long carrier diffusion lengths, and high carrier mobility.[1–8] Indeed, significant progress has been achieved in organic–inorganic hybrid perovskite based optoelectronics including highly sensitive photodetectors, broadband tunable light-emitting diodes (LEDs), highly efficient solar cells with power conversion efficiencies exceeding 20%, *etc.*[9–16] Nevertheless, the environmental instability of organic–inorganic hybrid perovskites is still the main concern for their practical applications. To overcome this hurdle, many all-inorganic halide perovskites have been developed as alternative materials.[17–28] Among these materials, tin (Sn) based perovskites $ASnX_3$ (X = I, Br, Cl) have attracted particular interest due to their

nontoxicity and excellent optoelectronic properties.[26–28] However, $ASnX_3$ are very sensitive to the ambient atmosphere (oxygen, moisture, *etc.*) and easily oxidized from Sn^{2+} to Sn^{4+}. Therefore, exploration of air-stable alternatives has become an urgent need. Very recently, chemically stable Sn^{4+} based vacancy-ordered double perovskite materials such as $Cs_2SnI_xCl_{6-x}$ and $Cs_2SnCl_{6-x}Br_x$ have been demonstrated for energy harvesting, light emitting, and narrow band light detection applications.[29–31] Unfortunately, the sensitivity of photodetectors fabricated from $Cs_2SnCl_{6-x}Br_x$ single crystals is limited ($<10^{11}$ Jones), and the detection range is restricted within the visible region. One possible approach for improving the performance of inorganic perovskite photodetectors is to combine the perovskite layer with other functional materials to form bilayer hetero-structures. For example, Tong *et al.* developed a sensitive, self-driven near infrared photodetector based on a $CsBi_3I_{10}$ perovskite/silicon heterojunction structure, very recently a Cs_2SnCl_6/GaN heterojunction photodetector has been demonstrated with excellent narrow-band sensitivity in the UV region.[32,33] A major challenge in designing a heterojunction photodetector is the need to improve the photoresponse of the device while at the same time maintaining a low dark current, which is critical for achieving high detectivity. Among many of the potential semiconductor materials for constructing a heterojunction with a perovskite, ZnO is a promising candidate due to its excellent

[a] *Department of Electrical, Computer, and Systems Engineering, Rensselaer Polytechnic Institute, Troy, NY 12180, USA. E-mail: shaodali828@gmail.com, sawyes@rpi.edu*

[b] *Department of Mechanical, Aerospace and Nuclear Engineering, Rensselaer Polytechnic Institute, Troy, NY 12180, USA. E-mail: lianj@rpi.edu*

[c] *Department of Chemical and Biological Engineering, Rensselaer Polytechnic Institute, Troy, NY 12180, USA*

This journal is © The Royal Society of Chemistry 2020

J. Mater. Chem. C, 2020, 8, 1819–1825 | **1819**

optical and electrical properties including a wide direct band gap (3.37 eV), large exciton binding energy (60 meV), high carrier mobility, and outstanding environmental stability.[34,35] In fact, for the same reason, ZnO has frequently been employed as an electron transfer layer in the fabrication of perovskite solar cells.[36–38] Among many different methods to grow ZnO thin films, the atomic layer deposition (ALD) technique has great potential in the fabrication of inorganic perovskite-based heterojunction photodetectors. ALD can provide thickness-controlled, dense and uniform thin films with minimum defects, which is critical to enhance the photocurrent and suppress the dark current for heterojunction optoelectronic devices.[39–41] Remarkably, recent work done by G. Cen, *et al.* demonstrated a highly sensitive and stable CsPbBr$_3$ perovskite heterojunction photodetector by employing ALD as a powerful interfacial engineering technique for device performance tuning and optimization.[39]

In this work, we demonstrate a high performance UV–Vis dual-band photodetector based on a Cs$_2$SnI$_6$/ZnO heterojunction structure. By adjusting the polarity of the applied bias voltage, the photodetector can switch between two operation modes: (1) UV–Vis dual-band detection mode and (2) visible-blind UV detection mode. Such a unique function of this photodetector greatly extends its practical applications. Benefitting from the excellent carrier separation efficiency at the hetero-interface, the device achieved high detectivity in both UV (1.39×10^{12} Jones) and visible (5.88×10^{11} Jones) regions. Furthermore, the photodetector demonstrated a fast response speed with a rise and fall time on the order of milliseconds and a large linear dynamic range of 119 dB. The results in this work demonstrate the great application potential of inorganic vacancy-ordered perovskites in high performance heterojunction photodetectors. Further research toward this direction is highly desirable.

Results and discussion

Fig. 1a shows the three-dimensional schematic illustration of the Cs$_2$SnI$_6$/ZnO heterojunction photodiode. The crystal structure of the vacancy-ordered double perovskite Cs$_2$SnI$_6$ is illustrated in Fig. 1b, which presents a vacancy-ordered double perovskite structure with isolated [SnI$_6$] octahedra. The scanning electron microscopy (SEM) image of the synthesized Cs$_2$SnI$_6$ NP thin film is shown in Fig. 1c, and the average size of the Cs$_2$SnI$_6$ NPs is estimated to be 20–30 nm. XRD was performed on the sample to check the crystallinity, as shown in Fig. 1d. The major peaks at the 2θ values: 13.2°, 15.2°, 21.6°, 25.4°, 26.6°, 30.8°, 44.1°, 52.0°, and 54.6°, correspond to the atomic planes of (111), (002), (022), (113), (222), (004), (044), (226), and (444), respectively. The UV–Vis absorption spectrum and the photoluminescence (PL) spectrum of the Cs$_2$SnI$_6$ NPs at room temperature are presented in Fig. 1e. The absorption spectrum shows a cut off wavelength at 860 nm, corresponding to an optical band gap of $\sim$1.4 eV. This optical band gap was further verified by PL spectroscopy. As shown in Fig. 1e, the PL spectrum excited at 520 nm exhibited a pronounced PL peak ranging from 770 to 1000 nm with the peak centered at 861 nm, confirming the effective optical band gap of $\sim$1.4 eV for the synthesized Cs$_2$SnI$_6$ NPs. This is consistent with previous literature reports, where the bandgap values vary from 1.26 to 1.6 eV.[42–44] It is worth mentioning that the post growth hydrogen annealing treatment of the ALD grown ZnO thin film can greatly improve the film conductivity due to the introduction of shallow donor states such as the VO–H complex and interstitial hydrogen.[45–47] In addition, the passivation effect of the post growth hydrogen annealing treatment can effectively cure the deep level defects and reduce the number of carrier scattering centers in the ZnO thin film, leading to improved electron mobility.[48] As demonstrated in Fig. 1f, the photoluminescence spectrum of the ZnO thin film after the hydrogen annealing

Fig. 1 (a) Schematic illustration of the Cs$_2$SnI$_6$/ZnO heterojunction photodiode. (b) Schematic illustration showing the crystal structure of the vacancy-ordered double perovskite Cs$_2$SnI$_6$. (c) SEM image of the Cs$_2$SnI$_6$ NP thin film. (d) XRD pattern of the synthesized Cs$_2$SnI$_6$ NPs. (e) UV–Vis absorption spectrum and PL spectrum of the synthesized Cs$_2$SnI$_6$ NPs. (f) PL spectra of the ALD grown ZnO thin film before (red line) and after (blue line) hydrogen annealing.

1820 | *J. Mater. Chem. C*, 2020, **8**, 1819–1825
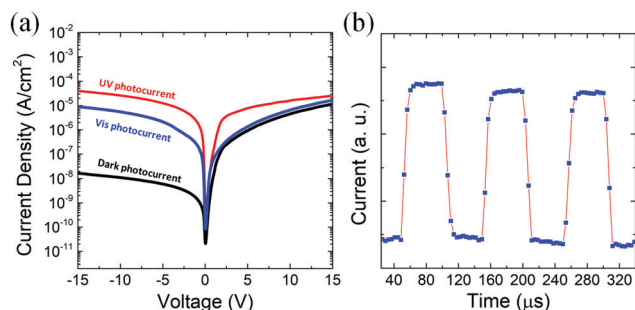
This journal is © The Royal Society of Chemistry 2020

Fig. 2 (a) I–V characteristics of the photodetector measured in the dark, under 760 nm visible illumination, and 375 nm UV illumination. (b) Transient response of the heterojunction photodiode with a rising time of 4.3 μs and a falling time of 5.2 μs measured under ambient conditions.

treatment shows greatly enhanced band-edge UV emission centered at ∼375 nm and suppressed defect level green emission centered at ∼600 nm.

The I–V characteristics of the photodetector are measured in the dark, under 760 nm visible illumination, and under 375 nm UV illumination, as shown in Fig. 2a. The dark current of the heterojunction photodiode shows an excellent rectifying characteristic with a high rectification ratio of 161 when biased at ±5 V. When forward biased, the dark current increases exponentially following the equation $I \sim \exp(\alpha V)$. The constant α is calculated to be 0.34 V^{-1} by fitting the experimental data. Under reverse bias, the photocurrent generated by 760 nm visible/375 nm UV illumination is over 500 times/three orders of magnitude higher than the dark current, demonstrating a good signal to noise ratio of this device in both the UV and visible region. Under forward bias, however, the photocurrent generated by 375 nm UV light is less than two orders of magnitude higher than the dark current, and the photocurrent generated by 760 nm visible light is almost comparable to the

dark current, suggesting a complete quenching of the photoresponse in the visible region. Such a kind of voltage polarity dependent photosensitivity will be discussed in detail later in this paper. The transient photoresponse of this device was measured under a 375 nm short pulse light from a LED, as presented in Fig. 3f. The rise time (output signal changing from 10% to 90% of the peak output value) and the decay time (output signal changing from 90% to 10% of the peak output value) of the photocurrent are 4.3 μs and 5.2 μs, respectively. This is faster than most of the perovskite based photodetectors reported so far, indicating good quality of the ZnO thin film and the Cs_2SnI_6 NPs.

Photoresponsivity is an important figure-of-merit for photodetectors, which is defined as the photocurrent per unit of incident optical power. The photoresponsivity and EQE pseudo-color maps of this heterojunction photodiode measured under reverse bias and forward bias conditions are shown in Fig. 3a and b, respectively. As shown in Fig. 3a, the photoresponsivity and EQE pseudo-color maps of this device under reverse bias show two major detection bands. The first detection band is contributed by the ZnO layer and is located in the UV region from 280 nm to 385 nm. A maximum photoresponsivity of 183.4 mA W^{-1} was measured at 378 nm wavelength, corresponding to an EQE of 60.2%. The second detection band located in the visible region from ∼600–900 nm is mainly contributed by the Cs_2SnI_6 layer. A maximum responsivity of 113.4 mA W^{-1} was measured at 858 nm (1.44 eV) wavelength, which agrees well with the bandgap of Cs_2SnI_6 (1.4 eV) measured in this work. Under forward bias, however, only the UV detection band remains while the visible detection band was completely quenched, as shown in Fig. 3b. A maximum responsivity of 108 mA W^{-1} at 374 nm was measured under forward bias, lower than that measured under reverse bias conditions. To understand this voltage polarity dependent photoresponse,

Fig. 3 (a) Photoresponsivity (top) and EQE (bottom) pseudo-color maps of this heterojunction photodiode measured under reverse bias voltages. (b) Photoresponsivity (top) and EQE (bottom) pseudo-color maps of this heterojunction photodiode measured under forward bias voltages. (c) Schematic energy band diagram showing the band alignment and carrier dynamics of this device operating under reverse bias (top) and forward bias (bottom) conditions.

we can refer to the schematic energy band diagram of this heterojunction shown in Fig. 3c. Based on the Anderson's model, the Cs_2SnI_6/ZnO heterojunction has a small conduction band offset of 0.4 eV and a large valence band offset of 1.6 eV. Since ZnO is highly transparent to visible light, most of the visible light can get through ZnO and be absorbed in the Cs_2SnI_6 film to generate electron-hole pairs (EHPs). Under reversed bias conditions, the photogenerated electrons at the Cs_2SnI_6 side can transport through the interfacial barrier easily (due to the small conduction band offset) and drift toward the contact at the ZnO thin film side driven by an external electrical field. At the same time, the photogenerated holes in both ZnO and Cs_2SnI_6 drift toward the contact at the Cs_2SnI_6 side without any energy barriers. Therefore, the photogenerated electrons and holes in both ZnO and Cs_2SnI_6 can be collected to form the photocurrent signal, resulting in the UV–Vis dual detection band. In contrast, when the heterojunction is forward biased, the photogenerated holes in the Cs_2SnI_6 side tend to drift toward the ZnO region under an external electrical field but they cannot get through the interfacial region due to the high energy barrier (1.6 eV) present for holes. Therefore, without any efficient charge separation at the hetero-interface under forward bias, the photogenerated holes in the Cs_2SnI_6 quickly recombine with the photogenerated electrons, leading to the significant quenching of the photo-response in the visible band. Therefore, by adjusting the polarity of external bias, our device can operate in either the UV–Vis dual detection band mode or the visible-blind UV detection mode. This function greatly extends the photodetector's practical applications including secure space-to-space communications, pollution monitoring, water sterilization, flame sensing, early missile plume detection, security surveillance, *etc.*

Detectivity (D^*) is an important parameter that indicates the ability of a photodetector to measure weak optical signals. The D^* is expressed as:[49,50]

$$D^* = \frac{\sqrt{AB}}{\text{NEP}}$$

where the NEP $= i_n/R$ is the noise equivalent power, A is the area of the device, B is the bandwidth, i_n is the measured noise current, and R is the photoresponsivity of the photodetector. The total noise current values of the photodetector measured at various frequencies (range from 1 Hz to 5 kHz) and at different dark current levels are presented in Fig. 4a and b, respectively. As shown in Fig. 4a, the device shows a small noise current below 1.5×10^{-1} pA Hz$^{-1/2}$ and slowly decreases to 4×10^{-2} pA Hz$^{-1/2}$ at the frequency of 5000 Hz, indicating that the $1/f$ noise of the device is not the main contributor to the total noise current. Generally, shot noise or thermal noise dominates the total noise in perovskite photodetectors. The shot noise $i_{n,s}$ can be expressed as:

$$i_{n,s} = \sqrt{2ei_d B}$$

where e is the element charge and i_d is the dark current of the device, and the thermal noise $i_{n,t}$ can be expressed as:

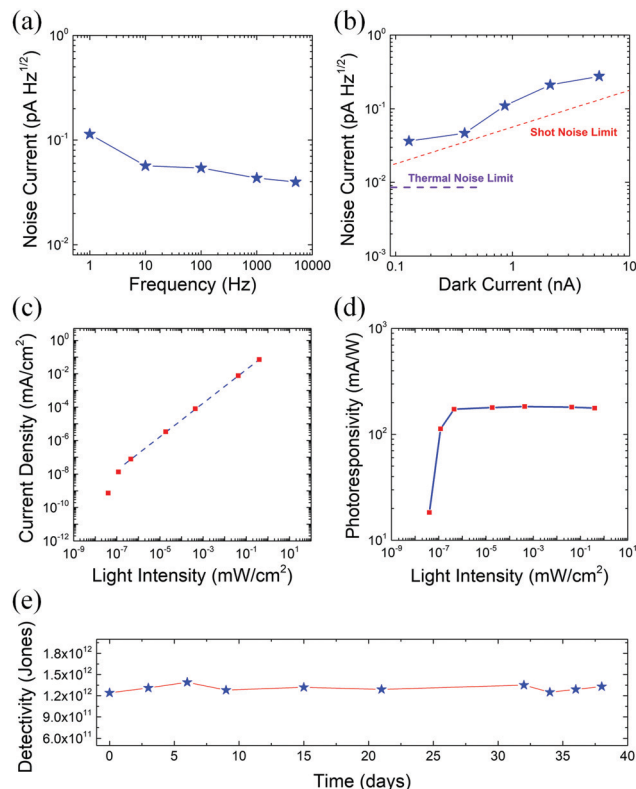$$i_{n,t} = \sqrt{(4k_B TB)/R}$$

Fig. 4 (a) Noise current measured at various frequencies in the range from 1 Hz to 5 kHz. (b) Noise current measured at different dark current levels. (c) Photocurrent density measured at varying light intensities. (d) The consistency of the photoresponsivity measured over a wide range of light intensity. (e) The detectivity of the photodetector measured over time.

where k_B is the Boltzmann constant, T is the temperature, and R is the resistance of the device. The shot noise limit and thermal noise limit of this device are plotted in Fig. 4b. Clearly, the total noise of this device is mainly dominated by the shot noise. In the UV region, a maximum specific detectivity of 1.39×10^{12} Jones was achieved at 378 nm and in the visible region, a maximum detectivity of 5.88×10^{11} Jones was measured at 858 nm, demonstrating excellent sensitivity of this heterojunction photodetector in both the UV and visible region. It is worth mentioning that the performance of the photodetector could be further improved through optimization of the Cs_2SnI_6 and ZnO layer thickness, which impacts the carrier recombination rate, carrier collection efficiency, and response speed of the photodetector.

In addition to the high detectivity, a constant responsivity from strong light all the way down to weak light is important for a detector so that it can be applied for weak light sensing. Every photodetector has a finite range of linear response and is characterized by a linear dynamic range, in which the responsivity remains constant. LDR is expressed as:[49,50]

$$\text{LDR} = 20 \log \left(\frac{P_{\text{high}}}{P_{\text{low}}} \right)$$

where P_{high} and P_{low} are the upper and lower limit of the incident light intensities and the photocurrent begins to deviate

1822 | *J. Mater. Chem. C*, 2020, **8**, 1819–1825

This journal is © The Royal Society of Chemistry 2020

Table 1 Performance comparison of inorganic perovskite heterojunction photodetectors in previous literature

Device structure	Measurement wavelength [nm]	Maximum responsivity [mA W^{-1}]	Rise/decay time [μs]	Detectivity [Jones]	LDR [dB]	Ref.
SnO$_2$/CsPbBr$_3$	300	380	N/A	2.6×10^{11}	N/A	52
Cs$_2$SnCl$_6$/GaN	378	208	0.75/0.91	1.2×10^{12}	71	33
CsPbBr$_3$/ZnO	450	4250	210/240	N/A	N/A	36
CsBi$_3$I$_{10}$/silicon	808	492.1	73/76	1.38×10^{11}	N/A	32
CsPbBr$_3$/InGaZnO	365	3794	2000/2000	NA	N/A	53
Al$_2$O$_3$/CsPbBr$_3$/TiO$_2$	405	440	28/270	1.88×10^{13}	~173	39
Cs$_2$SnI$_6$/ZnO	378	183.4	4.3/5.2	1.39×10^{12}	119	This work

from linearity beyond this range. The LDR of the heterojunction photodiode was characterized by measuring the photocurrent at a fixed frequency of 10 Hz under 375 nm UV illumination with varying light intensities from 4×10^{-8} mW cm^{-2} to 4×10^{-1} mW cm^{-2}, as shown in Fig. 4c. The photodetector demonstrated a linear photoresponse within the light intensity range from 4.5×10^{-7} mW cm^{-2} to 4×10^{-1} mW cm^{-2}, corresponding to an LDR of 119 dB. This is comparable to the LDR of Si photodetectors and is better than that of other types of photodetectors such as GaN (50 dB) and InGaAs (66 dB).[51] Fig. 4d shows the photoresponsivity measured within the above light intensity range, which shows a good consistency of the responsivity within the light intensity range from 4.5×10^{-7} mW cm^{-2} to 4×10^{-1} mW cm^{-2}. The detectivity of the photodetector over time is shown in Fig. 4e, and no obvious detectivity degradation is observed for more than 35 days after storage under 45% relative humidity conditions. The performance comparison of inorganic perovskite heterojunction photodetectors in previous literatures are shown in Table 1.
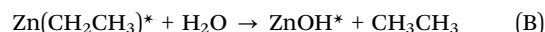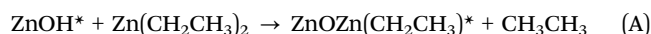
Conclusions

In conclusion, we demonstrated a Cs$_2$SnI$_6$/ZnO heterojunction photodetector with a high performance UV–Vis dual-band sensing capability. The photodetector can switch between the UV–Vis dual-band detection mode and visible-blind UV detection mode by adjusting the polarity of the external bias. This unique function of this photodetector greatly extends its practical applications. Benefitting from the excellent carrier separation efficiency at the hetero-interface, the device achieved high detectivity in both the UV (1.39×10^{12} Jones) and visible (5.88×10^{11} Jones) regions under reverse bias conditions. Furthermore, the photodetector demonstrated a fast response speed with a rise and fall time on the order of microseconds and a large linear dynamic range of 119 dB. The results in this work will be of particular interest for the future development of inorganic vacancy-ordered perovskite based high performance heterojunction photodetectors.

Experimental section

Growth of ZnO thin film

A ZnO thin film was grown on an ITO substrate through an atomic layer deposition (ALD) method (PICOSUN™ R-200 Advanced ALD system) with alternating diethylzinc and H$_2$O exposures:

$$ZnOH^* + Zn(CH_2CH_3)_2 \rightarrow ZnOZn(CH_2CH_3)^* + CH_3CH_3 \quad (A)$$

$$Zn(CH_2CH_3)^* + H_2O \rightarrow ZnOH^* + CH_3CH_3 \quad (B)$$

where the asterisks represent the surface species. By repeating these reactions in an ABAB... sequence, the ZnO layer can be deposited with atomic layer control. The ZnO ALD reaction sequence was: (i) dose diethylzinc to 1.0 Torr for 120 seconds; (ii) evacuate the reaction products and excess diethylzinc; (iii) dose N$_2$ to 20.0 Torr for 60 seconds and then evacuate N$_2$ (repeat 5 times); (iv) dose H$_2$O to 1.0 Torr for 120 seconds, (v) evacuate the reaction products and excess H$_2$O; (vi) dose N$_2$ to 20.0 Torr for 60 seconds and then evacuate N$_2$ (repeat 5 times). This sequence constitutes one AB cycle of ZnO ALD. The ZnO ALD was performed at 150 °C with 500 cycles and the thickness of the ZnO thin film is around 100 nm. Finally, the ITO substrate with an ALD grown ZnO thin film is placed in a furnace for post-annealing treatment in Ar/H$_2$ (ratio, 96:4) atmosphere at 400 °C for 2 hours.

Synthesis of perovskite NPs

Synthesis of Cs$_2$SnI$_6$ nanoparticles was done using a reverse injection process based on metal ion metathesis. First, 0.125 g SnI$_4$ was dissolved in dried octadecene (ODE) at 60 °C. Cs-precursor was prepared by dissolving 0.082 g of Cs$_2$CO$_3$ in 0.5 mL of OLAH, 5 mL ODE, and 0.5 mL of OLAM by heating at 130 °C for 1.5 h. Then the Cs-precursor was heated to 200 °C under vigorous stirring followed by the injection of SnI$_4$ solution. The colour of the precursor immediately changed to brown. The reaction was continued for 1 hour and quenched by adding the product into dichlorobenzene. Then, the brown precipitate (Cs$_2$SnI$_6$ NPs) was washed using dichlorobenzene in a centrifuge at 3500 rpm for 20 min twice followed by drying in an oven at 60 °C overnight.

Fabrication of the Cs$_2$SnI$_6$/ZnO heterojunction photodetector

For the device fabrication, the Cs$_2$SnI$_6$ NPs were dispersed in dichlorobenzene solvent and spin coated to the top of the ZnO thin film grown on an ITO substrate at a speed of 3000 rpm three times. The thickness of the Cs$_2$SnI$_6$ NP thin film is ~300 nm. Then an Al contact with a thickness of ~200 nm was deposited on the top of the device using an e-beam evaporator. Finally, the photodetector was packaged and the wire was bonded using Epo-Tek H20E conductive epoxy. The effective device area is 0.16 cm^2 defined by the shadow mask.

Material and device characterization

The SEM images of the Cs_2SnI_6 NPs were taken using a Carl Zeiss Ultra 1540 dual beam SEM. The XRD patterns of the Cs_2SnI_6 NPs were measured using a Bruker D8-Discover X-ray diffractometer. The UV–visible absorption spectrum of the Cs_2SnI_6 NPs was measured using a Shimadzu UV–Vis 2550 spectrophotometer. The PL spectrum of the Cs_2SnI_6 NPs was measured using a home-built system with a continuous wave diode laser (532 nm) and a Si photodetector. The PL spectrum of the ZnO thin film was measured using a Spex-Fluorolog-Tau-3 spectrofluorometer with the excitation wavelength fixed at 330 nm. The I–V characteristics of the Cs_2SnI_6/ZnO heterojunction photodetector were measured using a HP4155B semiconductor parameter analyser and LEDs with center peak wavelengths at 760 nm and 375 nm, respectively. The photoresponsivity and EQE pseudo-color maps of the device as a function of bias voltage were measured using a Shimadzu UV–Vis 2550 spectrophotometer in connection with a commercial optical power meter. The total noise current of the photodetector at room temperature was directly measured with an SR830 lock-in amplifier at different dark current levels and at various frequencies (ranging from 1 Hz to 5 kHz).

Conflicts of interest

The authors declare no conflict of interest.

Acknowledgements

Notes and references

1 S. D. Stranks, G. E. Eperon, G. Grancini, C. Menelaou, M. J. P. Alcocer, T. Leijtens, L. M. Herz, A. Petrozza and H. J. Snaith, *Science*, 2013, **342**, 341–344.

2 G. C. Xing, N. Mathews, S. Y. Sun, S. S. Lim, Y. M. Lam, M. Grätzel, S. Mhaisalkar and T. C. Sum, *Science*, 2013, **342**, 344–347.

3 J. Miao and F. Zhang, *J. Mater. Chem. C*, 2019, **7**, 1741–1791.

4 Y. Dong, Y. Zou, J. Song, X. Song and H. Zeng, *J. Mater. Chem. C*, 2017, **5**, 11369–11394.

5 J. Albero and H. García, *J. Mater. Chem. C*, 2017, **5**, 4098–4110.

6 L. Qiu, J. Deng, X. Lu, Z. Yang and H. Peng, *Angew. Chem., Int. Ed.*, 2014, **53**, 1–5.

7 I. E. Rauda, R. Senter and S. H. Tolbert, *J. Mater. Chem. C*, 2013, **1**, 1423–1427.

8 C. Han, H. Yu, J. Duan, K. Lu, J. Zhang, M. Shao and B. Hu, *J. Mater. Chem. C*, 2018, **6**, 6164–6171.

9 X. Hu, X. Zhang, L. Liang, J. Bao, S. Li, W. Yang and Y. Xie, *Adv. Funct. Mater.*, 2014, **24**, 7373–7380.

10 Z.-K. Tan, R. S. Moghaddam, M. L. Lai, P. Docampo, R. Higler, F. Deschler, M. Price, A. Sadhanala, L. M. Pazos, D. Credgington, F. Hanusch, T. Bein, H. J. Snaith and R. H. Friend, *Nat. Nanotechnol.*, 2014, **9**, 687–692.

11 G. Li, Z.-K. Tan, D. Di, M. L. Lai, L. Jiang, J. H.-W. Lim, R. H. Friend and N. C. Greenham, *Nano Lett.*, 2015, **15**, 2640–2644.

12 L. Dou, Y. Yang, J. You, Z. Hong, W.-H. Chang, G. Li and Y. Yang, *Nat. Commun.*, 2014, **5**, 5404.

13 M. I. Saidaminov, V. Adinolfi, R. Comin, A. L. Abdelhady, W. Peng, I. Dursun, M. Yuan, S. Hoogland, E. H. Sargent and O. M. Bakr, *Nat. Commun.*, 2015, **6**, 8724.

14 Y. Fang, Q. Dong, Y. Shao, Y. Yuan and J. Huang, *Nat. Photonics*, 2015, **9**, 679–686.

15 W. S. Yang, J. H. Noh, N. J. Jeon, Y. C. Kim, S. Ryu, J. Seo and S. I. Seok, *Science*, 2015, **348**, 1234–1237.

16 N. Arora, M. I. Dar, A. Hinderhofer, N. Pellet, F. Schreiber, S. M. Zakeeruddin and M. Grätzel, *Science*, 2017, **358**, 768–771.

17 H. Chen, A. Guo, J. Zhu, L. Cheng and Q. Wang, *Appl. Surf. Sci.*, 2019, **465**, 656–664.

18 L. Xu, Y. Wan, H. Xie, Y. Huang, L. Yang, L. Qin and H. J. Seo, *Appl. Surf. Sci.*, 2016, **389**, 849–857.

19 M. Kulbak, D. Cahen and G. Hodes, *J. Phys. Chem. Lett.*, 2015, **6**, 2452–2456.

20 A. Swarnkar, A. R. Marshall, E. M. Sanehira, B. D. Chernomordik, D. T. Moore, J. A. Christians, T. Chakrabarti and J. M. Luther, *Science*, 2016, **354**, 92–95.

21 L. Protesescu, S. Yakunin, M. I. Bodnarchuk, F. Krieg, R. Caputo, C. H. Hendon, R. X. Yang, A. Walsh and M. V. Kovalenko, *Nano Lett.*, 2015, **15**, 3692–3696.

22 J. Song, J. Li, X. Li, L. Xu, Y. Dong and H. Zeng, *Adv. Mater.*, 2015, **27**, 7162–7167.

23 X. Zhang, B. Xu, J. Zhang, Y. Gao, Y. Zheng, K. Wang and X. W. Sun, *Adv. Funct. Mater.*, 2016, **26**, 4595–4600.

24 X. Li, Y. Wu, S. Zhang, B. Cai, Y. Gu, J. Song and H. Zeng, *Adv. Funct. Mater.*, 2016, **26**, 2435–2445.

25 J. Duan, H. Xu, W. E. I. Sha, Y. Zhao, Y. Wang, X. Yang and Q. Tang, *J. Mater. Chem. C*, 2019, **7**, 21036–21068.

26 G. Nasti and A. Abate, *Adv. Energy Mater.*, 2019, 1902467.

27 N. K. Noel, S. D. Stranks, A. Abate, C. Wehrenfennig, S. Guarnera, A. Haghighirad, A. Sadhanala, G. E. Eperon, S. K. Pathak, M. B. Johnston, A. Petrozza, L. M. Herz and H. J. Snaith, *Energy Environ. Sci.*, 2014, **7**, 3061–3068.

28 F. Hao, C. C. Stoumpos, D. H. Cao, R. P. H. Chang and M. G. Kanatzidis, *Nat. Photonics*, 2014, **8**, 489–494.

29 B. Lee, C. C. Stoumpos, N. Zhou, F. Hao, C. Malliakas, C.-Y. Yeh, T. J. Marks, M. G. Kanatzidis and R. P. H. Chang, *J. Am. Chem. Soc.*, 2014, **136**, 15379–15385.

30 J. Zhou, J. Luo, X. Rong, P. Wei, M. S. Molokeev, Y. Huang, J. Zhao, Q. Liu, X. Zhang, J. Tang and Z. Xia, *Adv. Opt. Mater.*, 2019, **7**, 1900139.

31 Z. Tan, J. Li, C. Zhang, Z. Li, Q. Hu, Z. Xiao, T. Kamiya, H. Hosono, G. Niu, E. Lifshitz, Y. Cheng and J. Tang, *Adv. Funct. Mater.*, 2018, **28**, 1801131.

32 X.-W. Tong, Z.-X. Zhang, D. Wang, L.-B. Luo, C. Xie and Y.-C. Wu, *J. Mater. Chem. C*, 2019, **7**, 863–870.

33 D. Shao, W. Zhu, G. Xing, J. Lian and S. Sawyer, *Appl. Phys. Lett.*, 2019, **115**, 121106.

34 C.-Y. Chang, F.-C. Tsao, C.-J. Pan, G.-C. Chi, H.-T. Wang, J.-J. Chen, F. Ren, D. P. Norton, S. J. Pearton, K.-H. Chen and L.-C. Chen, *Appl. Phys. Lett.*, 2006, **88**, 173503.

35 D. C. Look, C. Coskun, B. Claflin and G. C. Farlow, *Physica B*, 2003, **340**, 32–38.

36 H. Liu, X. Zhang, L. Zhang, Z. Yin, D. Wang, J. Meng, Q. Jiang, Y. Wang and J. You, *J. Mater. Chem. C*, 2017, **5**, 6115–6122.

37 R. Zhang, C. Fei, B. Li, H. Fu, J. Tian and G. Cao, *ACS Appl. Mater. Interfaces*, 2017, **9**, 9785–9794.

38 D. Liu and T. L. Kelly, *Nat. Photonics*, 2014, **8**, 133–138.

39 G. Cen, Y. Liu, C. Zhao, G. Wang, Y. Fu, G. Yan, Y. Yuan, C. Su, Z. Zhao and W. Mai, *Small*, 2019, **15**, 1902135.

40 G. Yan, C. Zeng, Y. Yuan, G. Wang, G. Cen, L. Zeng, L. Zhang, Y. Fu, C. Zhao, R. Hong and W. Mai, *ACS Appl. Mater. Interfaces*, 2019, **11**, 32097–32107.

41 D. Shao, H. Sun, G. Xin, J. Lian and S. Sawyer, *Appl. Surf. Sci.*, 2014, **314**, 872–876.

42 B. Lee, C. C. Stoumpos, N. Zhou, F. Hao, C. Malliakas, C.-Y. Yeh, T. J. Marks, M. G. Kanatzidis and R. P. H. Chang, *J. Am. Chem. Soc.*, 2014, **136**, 15379–15385.

43 X. Qiu, B. Cao, S. Yuan, X. Chen, Z. Qiu, Y. Jiang, Q. Ye, H. Wang, H. Zeng, J. Liu and M. G. Kanatzidis, *Sol. Energy Mater. Sol. Cells*, 2017, **159**, 227–234.

44 B. Saparov, J.-P. Sun, W. Meng, Z. Xiao, H.-S. Duan, O. Gunawan, D. Shin, I. G. Hill, Y. Yan and D. B. Mitzi, *Chem. Mater.*, 2016, **28**, 2315–2322.

45 D. Shao, M. Yu, J. Lian and S. Sawyer, *Appl. Phys. Lett.*, 2012, **101**, 211103.

46 A. Janotti and C. G. Van de Walle, *Nat. Mater.*, 2007, **6**, 44–47.

47 P. F. Cai, J. B. You, X. W. Zhang, J. J. Dong, X. L. Yang, Z. G. Yin and N. F. Chen, *J. Appl. Phys.*, 2009, **105**, 083713.

48 J. B. Varley, H. Peelaers, A. Janotti and C. G. Van de Walle, *J. Phys.: Condens. Matter*, 2011, **23**, 334212.

49 C. Bao, Z. Chen, Y. Fang, H. Wei, Y. Deng, X. Xiao, L. Li and J. Huang, *Adv. Mater.*, 2017, **29**, 1703209.

50 Z. Yang, M. Le, M. Wang, K. Zhang, X. Li, J. Shao and W. Chen, *IEEE Sens. J.*, 2017, **17**, 4447–4453.

51 X. Gong, M. Tong, Y. Xia, W. Cai, J. S. Moon, Y. Cao, G. Yu, C. L. Shieh, B. Nilsson and A. J. Heeger, *Science*, 2009, **325**, 1665–1667.

52 Y. Zhang, W. Xu, X. Xu, J. Cai, W. Yang and X. Fang, *J. Phys. Chem. Lett.*, 2019, **10**, 836–841.

53 M. Sun, Q. Fang, Z. Zhang, D. Xie, Y. Sun, J. Xu, W. Li, T. Ren and Y. Zhang, *ACS Appl. Mater. Interfaces*, 2018, **10**(8), 7231–7238.

This journal is © The Royal Society of Chemistry 2020

J. Mater. Chem. C, 2020, **8**, 1819–1825 | 1825